

043

MAT

14551

**XENON PRODUCTION CROSS-SECTIONS ON BARIUM TARGETS BY  
ENERGETIC PROTONS FROM ACCELERATORS AND SIMULATION  
EXPERIMENTS ON MODEL METEOROIDS**

MATHEW K.J.

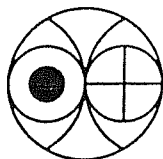
043



B14551

Ph. D. Thesis

JULY 1991



PHYSICAL RESEARCH LABORATORY

AHMEDABAD 380009

INDIA

043  
MAT  
14551

**XENON PRODUCTION CROSS-SECTIONS ON BARIUM TARGETS BY  
ENERGETIC PROTONS FROM ACCELERATORS AND SIMULATION  
EXPERIMENTS ON MODEL METEOROIDS**

*by*

Mathew K.J.

Physical Research Laboratory

Ahmedabad 380009, India

A thesis

submitted to the

Gujarat University

for the degree of

Doctor of Philosophy

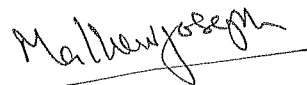
JULY 1991

PHYSICAL RESEARCH LABORATORY

AHMEDABAD 380009, INDIA

## CERTIFICATE


I hereby declare that the work presented in this thesis is original and has not formed the basis for the award of any degree or diploma by any University or Institution.



Mathew K.J.

(Author)

Certified by:



M.N.Rao

(Thesis Supervisor)

July 1991

## ABSTRACT

The primary objective of the work presented here is to experimentally determine the production cross-sections of xenon isotopes in proton induced reactions on barium targets by irradiation experiments using the low and high energy accelerators in Europe. For this purpose, both the "thin" and thick" target irradiation techniques have been employed. The proton energies used for these irradiations fall into two categories: (a) low (12 to 45 MeV) and (b) high (600 to 2600 MeV).

Based on the cross-section data covering a wide range of proton energies, obtained as a direct result of the present studies, excitation functions for the production of xenon isotopes in all energy regions are constructed. The excitation functions, thus obtained, can be used to calculate the SCR and GCR cosmogenic xenon production rates in moon and meteorite samples with the help of existing theoretical models. Here, SCR production rates of xenon isotopes on the lunar surface material are calculated and the production rate estimates are discussed together with the cross-section measurements.

The outline of the thesis is as follows.

Chapter I. Description of the energetic particles (GCR and SCR) in the interplanetary space and their interaction with extraterrestrial matter. Relevance of the simulation experiments in determining the cosmogenic production rates is emphasized and the various processes contributing to xenon in an extraterrestrial sample are briefed.

Chapter II. The mass spectrometric techniques are discussed in this Chapter, and the lunar rock samples studied here are described. Also discussed are the cosmic ray simulation irradiation experiments.

Chapter III. The results obtained in the low energy cross-section measurements are discussed. SCR xenon production rates in lunar surface material are elaborated. The results of the lunar rock xenon measurements are also discussed in the later parts of this Chapter.

Chapter IV. Here the results obtained in the high energy thin target proton irradiation experiments are discussed. The production rates of xenon isotopes measured in the diorite ( $R = 5$  cm) and gabbro ( $R = 26$  cm) spheres (thick target experiments) are also discussed in this Chapter.

Chapter V. Conclusions. In this concluding Chapter the results obtained during the course of the present work are summarised and the cosmochemical applications of the present results are discussed.

The results obtained in this study can be summarised as follows.

Our xenon production cross-section measurements on Ba targets in the proton energy range of  $12 \text{ MeV} < E < 45 \text{ MeV}$  show that in this low-energy range there is a significant production of Xenon isotopes. The isotopes  $^{129}\text{Xe}$ ,  $^{131}\text{Xe}$  and  $^{132}\text{Xe}$  are produced with larger abundance compared to the other xenon isotopes. For

example at ~24 MeV the production cross-sections of  $^{129}\text{Xe}$ ,  $^{131}\text{Xe}$  and  $^{132}\text{Xe}$  are, respectively,  $2.53 \pm 0.38$  mb,  $3.62 \pm 0.54$  mb and  $1.01 \pm 0.15$  mb, compared to the cross-section values of  $0.25 \pm 0.04$  mb for  $^{130}\text{Xe}$  and  $0.03 \pm 0.004$  mb for  $^{128}\text{Xe}$ . The relatively higher production cross-sections of these isotopes at proton energies of ~24 MeV indicate that pre-equilibrium  $\alpha$ -emission reaction channels involving barium targets are operational and these reactions favourably produce isotopes  $^{129}\text{Xe}$ ,  $^{131}\text{Xe}$ , and  $^{132}\text{Xe}$ .

The SCR production rates of xenon isotopes in lunar surface material are estimated using the cross-sections measured by us as input parameters in an existing model. These calculations show that the SCR xenon production rates estimated by us are ~ a factor 2 higher than the estimates available in literature. The surface production rates of  $^{132}\text{Xe}$  estimated in the present calculations are  $0.55 \times 10^{-15}$  ccSTP.g $^{-1}$ .Ma $^{-1}$ .ppmBa $^{-1}$  compared to the Hohenberg et al.,(1978) values of  $0.283 \times 10^{-15}$  ccSTP.g $^{-1}$ .Ma $^{-1}$ .ppmBa $^{-1}$ . This discrepancy is due to neglect of Xe production by low energy protons ( $E < 60$  MeV) in the earlier calculations. In an effort to deduce the solar cosmic ray produced Xe spectra in documented samples from oriented lunar rocks 61016, 64435 and 79215 the Xe concentrations measured in these rocks are deconvoluted into its constituent components. Our results show that in these rocks there are qualitative indications for the production of xenon isotopes  $^{129}\text{Xe}$ ,  $^{131}\text{Xe}$  and  $^{132}\text{Xe}$  by SCR protons. The SCR xenon spallation spectra deduced from these rocks is (large errors are associated with these numbers).

$$^{129}\text{Xe} : ^{131}\text{Xe} : ^{132}\text{Xe} = 0.94 : 2.30 : 1.00$$

In the high energy region, the production cross-sections for xenon isotopes on Ba targets (thin target irradiations) at proton energies of 600 MeV, 800 MeV, 1200 MeV and 2600 MeV are determined. In the energy range 600 MeV to 1200 MeV the production cross-sections of xenon isotopes remains more or less constant but at energies higher than 1200 MeV the production cross-sections decrease substantially. The  $^{126}\text{Xe}$  production cross-sections at 600, 800, and 1200 MeV are, respectively,  $54.5 \pm 3.8$  mb,  $85.4 \pm 6.0$  mb and  $65.5 \pm 5.0$  mb which are higher in comparison to the cross-section value of  $31.2 \pm 2.3$  mb at 2600 MeV. More significantly, the relative yields (spallation spectra) for the production of xenon isotopes change considerably in the proton energy region of  $600 \text{ MeV} < E < 2600 \text{ MeV}$  and this change is in such a way that the heavier isotope productions are enhanced with respect to the lighter xenon isotopes. The  $^{129}\text{Xe}/^{126}\text{Xe}$  and  $^{131}\text{Xe}/^{126}\text{Xe}$  isotopic ratios at 2600 MeV are, 1.420 and 1.901 as compared to 1.131 and 1.229 at 600 MeV.

In the "thick-target" experiments, we here found that xenon isotopes produced from barium glasses irradiated inside small sized bodies (i.e. diorite sphere,  $R = 5$  cm) do not show any variation as a function of depth. Based on these measurement, we conclude that the depth profiles for the production of cosmogenic xenon isotopes in small meteoroids (size  $\sim 5$  cm) in space are essentially flat.

Our results (thick target) from the measurement of Ba glasses irradiated inside gabbro sphere ( $R \sim 25$  cm) shows that there is a significant production of xenon isotopes from the secondary particles in the thick target bodies having radii,  $R \sim 25$

cm. The size effects are most pronounced in the case of isotope  $^{131}\text{Xe}$ . The production rates of  $^{131}\text{Xe}$  measured in Ba glass samples kept near the surface and near the center of the gabbro ( $R = 26$  cm) mock-up meteoroid are,  $7.65 \pm 1.15$  and  $4.6 \pm 0.70$  (both quantities in units of  $\times 10^{-10} \text{ccSTP.g}^{-1}.\text{Ma}^{-1}$ ). The corresponding values for isotope  $^{126}\text{Xe}$  are  $1.68 \pm 0.26$  and  $2.32 \pm 0.35$  (in units  $\times 10^{-10} \text{ccSTP.g}^{-1}.\text{Ma}^{-1}$ ). The enhanced production of this isotope is attributed to  $(n,\alpha)$  reactions on  $^{134}\text{Ba}$  and  $(n,2n)$  reactions on  $^{132}\text{Ba}$  target nuclide.

The production of xenon isotopes in proton induced reactions in extraterrestrial objects like moon and meteorites can be evaluated fairly accurately using the cross-section measurements obtained from the present study. For the first time we have a consistent set of xenon production cross-section measurements covering a wide range of energies  $12 \text{ MeV} < E < 2600 \text{ MeV}$ . However, it may be noted that, in the intermediate range (i.e.  $\sim 60$  to  $200 \text{ MeV}$ ), we had to use theoretically estimated cross-sections as there are no experimental xenon cross-sections available. In quantifying the cosmogenic production of xenon in moon and meteorite samples as well as deducing the other xenon components in these samples, this data base provided in this work is an important contribution.



	Page No.
ABSTRACT	(i)
ACKNOWLEDGEMENTS	(vi)
CONTENTS	(viii)
LIST OF TABLES	(xi)
LIST OF FIGURES	(xiv)
CHAPTER I INTRODUCTION	1
1.1 Nature of the Interacting particles in the interplanetary space	2
1.1a Galactic Cosmic Ray Particles	3
1.1b Solar Cosmic Ray Particles	6
1.2 Cosmogenic Nuclides : Scope of the study	6
1.2a Cosmogenic Nuclide Production Rates	7
1.2b Depth Profiles of Cosmogenic Nuclide Production : Thin and Thick target methods	10
1.2c Simulation Experiments	11
1.3 SCR Production Rate Model used here : basic approach	12
1.4 Xenon Components and its General Systematics	15
1.4a Trapped Xenon	19
1.4b Radiogenic Xenon	20
1.4c Spallation Xenon	22
1.4d Fission Xenon	24
1.5 Lunar rocks	26
CHAPTER II EXPERIMENTAL TECHNIQUES	28
2.1 Mass Spectrometric Techniques	28
2.1a The Ion Source	30

2.1b	Sector Magnetic Analyser	30
2.1c	Ion Detection and Measurement	31
2.2	Mass Spectrometer Characteristics	31
2.2a	Sensitivity	33
2.2b	Blank Corrections	36
2.2c	Mass Discrimination	36
2.3	Sample Analysing Procedure	37
2.3a	Gas extraction and Purification	38
2.4	Performance of the MS	40
2.5	Description of the Lunar rock samples	41
2.6	Irradiation Experiments	46
2.6a	Low Energy Irradiations	46
2.6b	Irradiation of the Model Meteoroid Spheres of Radii 5 cm and 26 cm	50
2.6c	Irradiation and Flux Monitoring	54
2.6d	Irradiations at Proton Energies of 800, 1200 and 260 MeV	57

### CHAPTER III RESULTS AND DISCUSSION - Part I (Low Energy)59

3.1	Low Energy Cross-section Measurements	60
3.1a	Analysis of the Data from Nuclear Spallation point of view	63
3.1b	Comparison of the present Results with existing cross-section measurements	74
3.2	SCR Xenon Production Rates on the Lunar Surface	78
3.2a	Comparison of the Present Calculations with Earlier estimates	98

3.2b	Concluding Remarks on the SCR Xenon Production Rate Calculations.	101
3.3	SCR Xenon Spallation Ratios Deduced from Study of Lunar Rocks 61016, 64435 and 79215.	103
3.3a	Discussion on the Lunar Rock Xenon Data	105
3.3b	SCR Spallation Spectra Inferred from Lunar Rocks 61016, 64435 and 79215	116
CHAPTER IV	RESULTS AND DISCUSSION - Part II (High Energy)	121
4.1	High energy measurements	121
4.1a	Thin target Production Cross-sections at xenon isotopes on Ba at Proton energies of 600, 800, 1200 and 2600 MeV.	122
4.1b	Thin target spallation yields at high energies	128
4.2	Production Profiles of Xe Isotopes as a function of depth in Model Meteoroids.	133
4.2a	Xenon Production Profiles (experimentally measured) in the 5 cm Diorite sphere.	136
4.2b	Xenon production Profiles (experimentally measured) in the 25 cm Gabbro Sphere	146
CHAPTER V	CONCLUSIONS	167
APPENDIX I		
APPENDIX II		
APPENDIX III		
APPENDIX IV		
REFERENCE		179
LIST OF PUBLICATIONS		192

## LIST OF TABLES

Table 2.1	Description of the rock samples studied.
Table 2.2	Depth positions of the rock samples analysed here.
Table 3.1	$^{132}\text{Xe}$ concentrations and isotopic composition of xenon produced in p-induced reactions on barium upto 45 MeV (PRL measurements).
Table 3.2	$^{132}\text{Xe}$ concentrations and isotopic composition of xenon produced in p-induced reactions on barium upto 45 MeV (NCC measurements)
Table 3.3	Nuclear reactions on barium targets resulting in production of various xenon isotopes.
Table 3.4	Measured production cross-section values ( $\sigma$ ) for $^{130}\text{Xe}$ in p-induced reactions on barium targets upto 45 MeV.
Table 3.5	Estimated xenon isotope production rates in lunar surface material upto shielding depth of $24 \text{ g.cm}^{-2}$ .
Table 3.6	$^{130}\text{Xe}$ concentrations and isotopic ratios of Xe measured in R1, R2 and R3 samples of lunar rock 61016.
Table 3.7	$^{130}\text{Xe}$ concentrations and isotopic ratios of Xe measured in R1, R2 and R3 samples of lunar rock 64435.
Table 3.8	$^{130}\text{Xe}$ concentrations and isotopic ratios of Xe measured in R1, R2 and R3 samples of lunar rock 79215.

Table 3.9	Solar cosmic ray produced xenon isotopes in Rock 61016.
Table 3.10	Solar cosmic ray produced xenon isotopes in Rock 64435.
Table 3.11	Solar cosmic ray produced xenon isotopes in Rock 79215.
Table 3.12	Deduced SCR produced $^{132}\text{Xe}$ concentrations and isotopic ratios of Xe in rocks 61016, 64435 and 79215.
Table 4.1	$^{126}\text{Xe}$ production cross-sections $[\sigma]$ and thin target spallation spectra of xenon at p-energies of 600, 800, 1200 and 2600 MeV.
Table 4.2	$^{126}\text{Xe}$ concentrations and isotopic composition of xenon, measured in the diorite sphere ( $R=5$ cm) irradiated isotropically with 600 MeV protons.
Table 4.3	Production rates of xenon isotopes from Ba targets measured at different depths inside the diorite ( $R=5$ cm) sphere irradiated isotropically with 600 MeV protons.
Table 4.4	Enhancement in xenon production rates due to secondary particles as a function of depth in the diorite sphere ( $R=5$ cm).
Table 4.5	$^{126}\text{Xe}$ concentrations and isotopic composition of xenon, measured in the gabbro sphere ( $R=25$ cm) irradiated with 600 MeV protons.

- Table 4.6      Production rates of xenon isotopes from Ba targets, measures at different depths inside the gabbro (R =25 cm) sphere irradiated with 600 MeV protons.
- Table 4.7      Enhancement in xenon production rates due to secondary particles as a function of depth in the gabbro sphere (R =25 cm).
- Table 4.8      Increase in production of  $^{126}\text{Xe}$  and change in isotopic ratios of Xe at various depths inside the gabbro sphere (R =25 cm) irradiated with 600 MeV protons.

## LIST OF FIGURES

- Figure 1.1      Energy ranges and penetrating depths of the energetic radiations in the interplanetary space.
- Figure 1.2      GCR proton energy spectra during periods of solar maxima and solar minima.
- Figure 1.3      SCR particle spectra as a function of shielding depth in lunar surface material.
- Figure 1.4      Xenon, its neighbouring elements and their isotopic abundances.
- Figure 1.5      Relative abundances of xenon in solar system material.
- Figure 1.6      Isotopic abundances of xenon in various solar system reservoirs.
- Figure 2.1      Schematic diagram of the Reynolds type mass spectrometer.
- Figure 2.2      Xenon peaks measured during a sample run.
- Figure 2.3      Typical xenon air spectrum measured by the MS.
- Figure 2.4      Mass discrimination of the various xenon isotopes.
- Figure 2.5      Schematic diagram of the noble gas extraction and purification system.
- Figure 2.6      Sketch of lunar rock 61016 describing positions of the analysed samples.
- Figure 2.7      Sketch of lunar rocks 61016 and 64435 describing the positions of the analysed samples.
- Figure 2.8      Schematic diagram of the stack arrangement for thin target irradiations.

- Figure 2.9 Experimental arrangement used for the thin/thick target irradiations.
- Figure 2.10 Sketch of the diorite sphere ( $R = 5$  cm) and its target cores.
- Figure 2.11 Movements of the diorite ( $R = 5$  cm) sphere during irradiation.
- Figure 3.1  $^{126}\text{Xe}$ ,  $^{128}\text{Xe}$ ,  $^{130}\text{Xe}$  and  $^{134}\text{Xe}$  production cross-sections on Ba targets for p-energies upto 45 MeV.
- Figure 3.2  $^{129}\text{Xe}$ ,  $^{131}\text{Xe}$ , and  $^{132}\text{Xe}$  production cross-sections on Ba targets for p-energies upto 45 MeV.
- Figure 3.3 Isotopic ratios  $^{129}\text{Xe}/^{130}\text{Xe}$ ,  $^{131}\text{Xe}/^{130}\text{Xe}$  and  $^{132}\text{Xe}/^{130}\text{Xe}$  for production of xenon isotopes for p-energies upto 45 MeV.
- Figure 3.4 Isotopic ratios  $^{126}\text{Xe}/^{130}\text{Xe}$ ,  $^{128}\text{Xe}/^{130}\text{Xe}$  and  $^{134}\text{Xe}/^{130}\text{Xe}$  for production of xenon isotopes for p-energies upto 45 MeV.
- Figure 3.5  $^{127}\text{Xe}$  production cross-sections on Ba targets for p-energies upto 45 MeV.
- Figure 3.6  $^{128}\text{Xe}$  production rate in lunar surface material as a function of shielding depth.
- Figure 3.7  $^{129}\text{Xe}$  production rate in lunar surface material as a function of shielding depth.
- Figure 3.8  $^{130}\text{Xe}$  production rate in lunar surface material as a function of shielding depth.
- Figure 3.9  $^{131}\text{Xe}$  production rate in lunar surface material as a function of shielding depth.



- Figure 3.10  $^{132}\text{Xe}$  production rate in lunar surface material as a function of shielding depth.
- Figure 3.11  $^{128}\text{Xe}$  production rate in lunar surface material calculated by various models.
- Figure 3.12  $^{129}\text{Xe}$  production rate in lunar surface material calculated by various models.
- Figure 3.13  $^{130}\text{Xe}$  production rate in lunar surface material calculated by various models.
- Figure 3.14  $^{131}\text{Xe}$  production rate in lunar surface material calculated by various models.
- Figure 3.15  $^{132}\text{Xe}$  production rate in lunar surface material calculated by various models.
- Figure 3.16  $^{124}\text{Xe}/^{130}\text{Xe}$ ,  $^{126}\text{Xe}/^{130}\text{Xe}$ ,  $^{128}\text{Xe}/^{130}\text{Xe}$  and  $^{129}\text{Xe}/^{130}\text{Xe}$  production ratios in lunar surface material as a function of depth.
- Figure 3.17  $^{131}\text{Xe}/^{130}\text{Xe}$ , and  $^{132}\text{Xe}/^{130}\text{Xe}$  production ratios as a function of depth in lunar surface material.
- Figure 4.1  $^{124}\text{Xe}$  and  $^{126}\text{Xe}$  production cross-sections on Ba targets for p-energies upto 2600 MeV.
- Figure 4.2  $^{128}\text{Xe}$  and  $^{130}\text{Xe}$  production cross-sections on Ba targets for p-energies upto 2600 MeV.
- Figure 4.3  $^{129}\text{Xe}$  and  $^{131}\text{Xe}$  production cross-sections on Ba targets for p-energies upto 2600 MeV.
- Figure 4.4  $^{132}\text{Xe}$  and  $^{134}\text{Xe}$  production cross-sections on Ba targets for p-energies upto 2600 MeV.

- Figure 4.5 Percentage deviation of the isotopic ratios of Xe for p-energies upto 2600 MeV.
- Figure 4.6 Xe spallation spectra at high energies.
- Figure 4.7a  $^{124}\text{Xe}$ ,  $^{126}\text{Xe}$  and  $^{128}\text{Xe}$  production rates as a function of depth in the diorite sphere ( $R = 5$  cm).
- Figure 4.7b  $^{130}\text{Xe}$  and  $^{132}\text{Xe}$  production rates as a function of depth in the diorite sphere ( $R = 5$  cm).
- Figure 4.8  $^{131}\text{Xe}$  and  $^{129}\text{Xe}$  production rates as a function of depth in the diorite sphere ( $R = 5$  cm).
- Figure 4.9 Percentage deviation of the measured spallation spectra in Ba glasses from diorite sphere ( $R = 5$  cm) from the thin target spallation spectra.
- Figure 4.10  $^{124}\text{Xe}/^{126}\text{Xe}$ ,  $^{128}\text{Xe}/^{126}\text{Xe}$  and  $^{129}\text{Xe}/^{126}\text{Xe}$  ratios as a function of depth in the diorite ( $R=5$  cm) sphere.
- Figure 4.11  $^{130}\text{Xe}/^{126}\text{Xe}$ ,  $^{131}\text{Xe}/^{126}\text{Xe}$  and  $^{132}\text{Xe}/^{126}\text{Xe}$  as a function of depth in the diorite ( $R=5$  cm) sphere.
- Figure 4.12  $^{124}\text{Xe}$ ,  $^{126}\text{Xe}$  and  $^{130}\text{Xe}$  production rates as a function of depth in the gabbro sphere ( $R = 26$  cm), irradiated with 600 MeV protons.
- Figure 4.13  $^{129}\text{Xe}$ , and  $^{131}\text{Xe}$  production rates as a function of depth in the gabbro sphere ( $R = 26$  cm), irradiated with 600 MeV protons.
- Figure 4.14  $^{132}\text{Xe}$ , and  $^{134}\text{Xe}$  production rates as a function of depth in the gabbro sphere ( $R = 26$  cm), irradiated with 600 MeV protons.

Figure 4.15 Percentage deviation of the spallation spectra measured in the gabbro sphere ( $R = 26$  cm) from the thin target spallation spectra.

Figure 4.16  $^{124}\text{Xe}/^{126}\text{Xe}$ ,  $^{128}\text{Xe}/^{126}\text{Xe}$  and  $^{129}\text{Xe}/^{126}\text{Xe}$  as a function of depth in the gabbro sphere ( $R=26$  cm) irradiated with 600 MeV protons.

Figure 4.17  $^{130}\text{Xe}/^{126}\text{Xe}$ ,  $^{131}\text{Xe}/^{126}\text{Xe}$  and  $^{132}\text{Xe}/^{126}\text{Xe}$  as a function of depth in the gabbro sphere ( $R=26$  cm) irradiated with 600 MeV protons.